SCIENCE CHINA
Technological Sciences

•Article•

April 2023 Vol.66 No.4: 1141–1151
https://doi.org/10.1007/s11431-022-2309-1

High-efficiency resistive switch and artificial synaptic simulation in antimony-based perovskite devices

LUO FeiFei[1], WU YanZhao[1], TONG JunWei[2], XU DaKe[1], QIN GaoWu[1], TIAN FuBo[3] & ZHANG XianMin[1*]

[1] *Key Laboratory for Anisotropy and Texture of Materials (Ministry of Education), School of Materials Science and Engineering, Northeastern University, Shenyang 110819, China;*
[2] *Department of Physics, Freie Universität Berlin, 14195 Berlin, Germany;*
[3] *State Key Laboratory of Superhard Materials, College of Physics, Jilin University, Changchun 130012, China*

Received October 14, 2022; accepted January 3, 2023; published online March 21, 2023

Three kinds of $Cs_3Sb_2X_9$ (X=I, Br, Cl) perovskite films have been prepared to fabricate the resistive memory devices with the structure of Al/$Cs_3Sb_2X_9$ (X=I, Br, Cl)/indium tin oxide (ITO) glass. All devices exhibited a bipolar resistive switching behavior at room temperature by applying scanning voltage of 0 → 1 → 0→ −1.8 → 0 V. The switching voltages in the Al/$Cs_3Sb_2X_9$ (X=I, Br, Cl)/ITO devices gradually decreased with the X from I, Br to Cl due to the different migration rates of halide vacancy in perovskite films, which is confirmed by the first-principles calculations of activation energy. The ON/OFF ratio under the reading voltage of 0.1 V significantly increased up to 100 in the Al/$Cs_3Sb_2Cl_9$/ITO device, which is nearly 10 and 3 times larger than that of the Al/$Cs_3Sb_2I_9$/ITO device and the Al/$Cs_3Sb_2Br_9$/ITO device, respectively. The endurance cycles and retention time of current devices were evaluated, showing the excellent electrical stability. Importantly, the three kinds of Al/$Cs_3Sb_2X_9$ (X=I, Br, Cl)/ITO device can successfully simulate the short-term plasticity of biological synapse. The Al/$Cs_3Sb_2Cl_9$/ITO device showed the highest paired-pulsed facilitation index compared with that of other two devices, which was explored for the long-term plasticity and learning experience processes of synapse. In addition, the Al/$Cs_3Sb_2Cl_9$/ITO device established associative learning behavior by simulating the Pavlov's dog experiment.

perovskite films, resistive switching, artificial synapse

Citation: Luo F F, Wu Y Z, Tong J W, et al. High-efficiency resistive switch and artificial synaptic simulation in antimony-based perovskite devices. Sci China Tech Sci, 2023, 66: 1141–1151, https://doi.org/10.1007/s11431-022-2309-1

1 Introduction

Resistive random-access memory (RRAM) has attracted increasing attention for future non-volatile memory applications. The core structure of RRAM is a resistive memory device, which is a multilayer device composed of two electrodes separated by a switching spacer layer [1–4]. Moreover, RRAM can be used as artificial synapse devices by modulating the conductance states of resistive memory devices to simulate biological synaptic behaviors [5–7]. The memory function of RRAM devices is dependent on the formation and rupture of the conductive filaments formed inside the switching layers by applying external electric fields. Therefore, the switching layers play a vital role to determine the performance of RRAM [8–10]. Traditionally, several kinds of materials have been used as the switching layer for memristor, including oxides, chalcogenides, and polymers [11,12]. In the recent years, perovskites have attracted more attention because of the advantages of long carrier diffusion length, tunable bandgap, large and bipolar carrier mobility [9,13]. The lead halide perovskites have been extensively utilized as the switching layers in RRAM,

*Corresponding author (email: zhangxm@atm.neu.edu.cn)

demonstrating the hysteretic current-voltage responses and artificial synaptic performance [11,14–17]. However, considering the inevitable toxicity of lead element, lead-free antimony halide perovskites is highly desirous. Among them, $Cs_3Sb_2X_9$ (X=I, Br, Cl) has drawn special interest because Sb^{3+} with ns^2 lone pairs of electrons is isoelectronic with Pb^{2+}, and thereby exhibiting an air stability through the screen-charged defects [18–20]. These characteristics of $Cs_3Sb_2X_9$ (X=I, Br, Cl) should be beneficial to the development of efficient and environmentally friendly memory devices.

The perovskites of $Cs_3Sb_2X_9$ (X=I, Br, Cl) with different sizes and morphologies have been studied in the past few years. The colloidal quantum dots or solid powders of $Cs_3Sb_2X_9$ (X=I, Br, Cl), such as $Cs_3Sb_2Br_9$ nanocrystals and nanoflakes, $Cs_3Sb_2Cl_9$ nanorods and nanowires, have been synthesized, which are promising for photocatalytic applications [18,21–25]. Meanwhile, Pradhan et al. [26] studied the structural phase transition and band gap engineering in $Cs_3Sb_2Cl_9$ by replacing Sb with Bi element. The heterovalent Mn-doped $Cs_3Sb_2Cl_9$ crystals were studied both experimentally and theoretically by Wang and co-authors [27]. In comparison, a two-step deposition approach was firstly proposed to grow $Cs_3Sb_2I_9$ film based on thermal evaporation techniques, which was used for photovoltaic cells [28]. Correa-Baena et al. [29] fabricated the $Cs_3Sb_2I_9$ film with a dimer phase for solar cells. The layered $Cs_3Sb_2I_9$ perovskite film grown by a HCl-assisted solution method could pronouncedly reduce the layer phase reaction temperature from 300°C to 160°C in contrast to traditional vapor solid reaction method [30]. Singh et al. [31] developed a layer polymorph of $Cs_3Sb_2I_9$ film through a vapor-assisted solution-processing to enhance the photovoltaic performance and increased the performance of dimer $Cs_3Sb_2I_9$ solar cells by Lewis-Pair Mediation [32]. Up to date, there are only a few of investigations for RRAM using the $Cs_3Sb_2X_9$ (X=I, Br, Cl) perovskites. Mao et al. [19] prepared a lateral-structured device using a $Cs_3Sb_2Br_9$ nanoflake, simulating the Ca^{2+} dynamic process of biological synapses. Recently, Paramanik et al. [33] reported the resistive switching and artificial synaptic behaviors of vertical-structured devices using the $Cs_3Sb_2I_9$ perovskite as an insulative layer. Unfortunately, the large switching voltages (V_{SET} and V_{RESET}) beyond 1 V and small endurance below 200 cycles in both devices seriously restrict the potential applications of antimony-based perovskite RRAM devices. Furthermore, it is still lack of a report about the dependence of halide ions in $Cs_3Sb_2X_9$ (X=I, Br, Cl) devices on the resistive switching and synaptic performance [13].

In this study, three kinds of $Cs_3Sb_2X_9$ (X=I, Br, Cl) perovskite films have been prepared by a vapor-anion-exchange method in a glove box, which were used to fabricate the resistive memory devices with the structure of Al/$Cs_3Sb_2X_9$ (X=I, Br, Cl)/ITO glass. The films were systematically characterized by X-ray diffractometer (XRD), X-ray photoelectron spectroscopy (XPS), Raman spectrum, scanning electron microscopy (SEM), and ultraviolet-visible (UV-vis) spectrum. Interestingly, all the present devices exhibited a bipolar resistive switching behavior at room temperature, showing both V_{SET} and V_{RESET} were far below 1 V with the endurance up to 750 cycles. The switching voltages in the Al/$Cs_3Sb_2X_9$ (X=I, Br, Cl)/ITO devices gradually decreased with the X from I, Br to Cl due to the different migration rates of halide vacancy in perovskite films, which is confirmed by the first-principles calculations of activation energy. The ON/OFF ratio under the reading voltage of 0.1 V significantly increased up to 100 in the Al/$Cs_3Sb_2Cl_9$/ITO device, which is nearly 10 and 3 times larger than that of the Al/$Cs_3Sb_2I_9$/ITO device and the Al/$Cs_3Sb_2Br_9$/ITO device, respectively. The endurance cycles and retention time of current devices were also evaluated, showing the excellent electrical stability. Importantly, the three kinds of Al/$Cs_3Sb_2X_9$ (X=I, Br, Cl)/ITO device can successfully simulate the short-term plasticity of biological synapse. Moreover, the Al/$Cs_3Sb_2Cl_9$/ITO device showed the highest paired-pulsed facilitation index compared with other two devices, which was very interesting and explored for the long-term plasticity and learning experience processes of synapse.

2 Experimental

2.1 Experimental materials

All chemicals and solvents were employed as received without any purification, including cesium iodide (CsI, 99.99%, Sigma-Aldrich), antimony (III) iodide (SbI_3, 99.999%, Sigma-Aldrich), antimony (III) bromide ($SbBr_3$, 99.99%, Sigma-Aldrich), antimony (III) chloride ($SbCl_3$, 99.99%, Sigma-Aldrich), dimethylsulfoxide (DMSO, 99.9%, Alfa Aesar), dimethylformamide (DMF, 99.9%, Alfa Aesar).

2.2 Films and device fabrications

First, the ITO substrates (1 cm × 1 cm) were cleaned orderly in deionized water, acetone, and anhydrous ethanol for 20 min under the condition of ultrasonication, followed cleaning by UV-O_3 for 20 min. Then, the preparation of the precursor solution was carried out by dissolving SbI_3 (0.25 mol/L) and CsI (1 mol/L) in a mixed solvent (DMSO: DMF, 9:1 volume ratio), and continuously stirring at 70°C for 6 h. This solution was spin-coated on the ITO substrates at 6000 r/min for 40 s. Next, these films were preheated at 70°C for 30 min and then moved to glass bottle. 20 μL of SbX_3 (X=I, Br, Cl) in DMF were added in the corners of the bottle, then, covering bottle with a cap. The films were

maintained at 200°C for 15 min to form $Cs_3Sb_2X_9$ (X=I, Br, Cl) films, and the thickness of perovskite films was approximately 200 nm. Figure 1 shows the schematic of the synthesis route of $Cs_3Sb_2X_9$ (X=I, Br, Cl) films. Finally, the Al electrodes (100 nm) were sputtered onto films to accomplish the Al/$Cs_3Sb_2X_9$ (X=I, Br, Cl)/ITO devices.

2.3 Characterization and analysis methods

The XRD from Japan Rigaku were applied to perform the crystal structures of perovskite films. The thickness of films was measured by the Profile-system from Vecco Dektak 150. The XPS from Shimazu-Kratos Analytical examined the chemical composition of films. The morphologies of perovskite films were observed by the SEM from JEOL JEM-7001F. The elemental mapping of the films was acquired by energy dispersive spectroscopy (EDS) from TESCAN MIRA3. The Raman spectra were obtained from LabRAM XploRA ONE spectrograph under 532 nm continuous-wave laser excitation. The UV-vis spectrum from Lambda 750S recorded the spectrum of the films. The current-voltage (*I-V*) behaviors were studied using a Keithley 2400, and artificial synaptic behaviors were measured by Keithley 2614B at room temperature. First-principles calculations based on density functional theory were carried out on Vienna *Ab initio* Simulation Package [34–36] by projector-augmented wave method [37,38]. The exchange-correlation functional was treated by the generalized gradient approximation based on the Perdew-Burke-Ernzerhof functional [39,40]. The kinetic energy cutoff was set at 550 eV. The convergence criteria of force and energy are 0.01 eV/Å and 10–6 eV, respectively. To determine the lattice parameters of $Cs_3Sb_2X_9$ (X=I, Br, Cl), their primitive cells were calculated with a Γ-centered 6×6×5 Monkhorst-Pack *k*-point grid. The minimum migration energy was calculated by nudged elastic band method [41]. The 2×2×2 $Cs_3Sb_2X_9$ (X=I, Br, Cl) supercells containing 112 atoms were constructed to calculate the activation energies of X (X=I, Br, Cl) vacancies with a 2×2×1 Γ-centered Monkhorst-Pack grid [42].

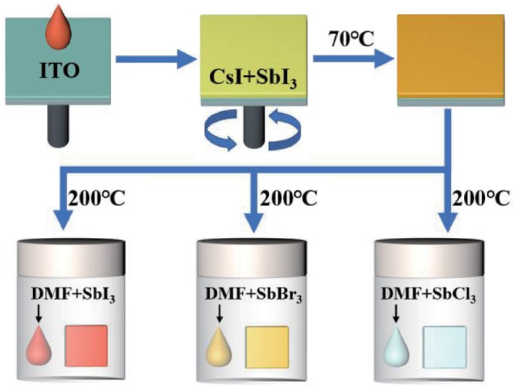

Figure 1 (Color online) Schematic of the synthesis route of $Cs_3Sb_2X_9$ (X=I, Br, Cl) films.

3 Discussion

3.1 Film characterizations

The crystal structures of $Cs_3Sb_2X_9$ (X=I, Br, Cl) films and ITO glass substrate for comparison were checked using the XRD measurements, as exhibited in Figure 2(a). Three peaks of $Cs_3Sb_2I_9$ film were clearly observed at 25.7°, 30.0°, and 43.4°, corresponding to the (003), (022), and (204) planes of triagonal phase, respectively [30]. This means that the crystallization of $Cs_3Sb_2I_9$ film is in the layer form, which is believed more stable for practical applications in electronic devices [43,44]. The dominant diffraction peaks of $Cs_3Sb_2Br_9$ film located at 22.5°, 27.5°, 32.0°, and 45.7°, which was assigned to the (012), (003), (022), and (204) planes of triagonal phase, respectively [24]. There were also four diffraction peaks for the $Cs_3Sb_2Cl_9$ film, locating at 23.4°, 28.8°, 33.3°, and 47.8°, which were consistent with the (110), (003), (022), and (204) planes of triagonal phase, respectively [27]. Interestingly, a continuous shift of XRD pattern peaks were observed in the (003), (022), and (204) planes of $Cs_3Sb_2X_9$ (X=I, Br, Cl) films. The shift resulted from the change of interplanar crystal spacings, which were mainly due to the anions size following the relation of I^->Br^->Cl^-. Additionally, there is not any diffraction peak from the CsI, demonstrating a perfect crystalline of the present $Cs_3Sb_2X_9$ (X=I, Br, Cl) films [28].

To further demonstrate the compositions of the three $Cs_3Sb_2X_9$ (X=I, Br, Cl) films, the XPS measurements were performed. Figure 2(b) showed the full-range XPS spectra of the $Cs_3Sb_2X_9$ (X=I, Br, Cl) films and the presence of Cs, Sb, and X was confirmed without any other element. The high-resolution XPS spectra of $Cs_3Sb_2X_9$ (X=I, Br, Cl) films were drawn in Figure S1, clearly showing the exact position of each binding energy peak. The binding energy peaks at both 618.1 and 630.1 eV were ascribed to I 3d and the peak at the low energy side ~48.7 eV was from I 4d in $Cs_3Sb_2I_9$ film. The binding energy peaks at both 181.1 and 187.9 eV resulted from Br 3p and the peaks at 68.2 and 69.0 eV were originated from Br 3d in $Cs_3Sb_2Br_9$ film. Meanwhile, Cl 2p peaks were located at 197.8 and 199.3 eV in $Cs_3Sb_2Cl_9$ film. The above binding energy peaks were well in agreement with the previous literatures [20,45]. Thus, the results of XPS measurement confirm that the $Cs_3Sb_2X_9$ (X=I, Br, Cl) films have been successfully synthesized, agreeing with the XRD results in Figure 2(a).

The Raman spectra of $Cs_3Sb_2X_9$ (X=I, Br, Cl) perovskite films were shown in Figure 2(c). $Cs_3Sb_2I_9$ exhibits a sharp peak at 150 cm^{-1}, which is due to the stretching of Sb–I bonds. There were two peaks locating at 180 and 210 cm^{-1} in the $Cs_3Sb_2Br_9$ film, corresponding to the vibrations of Sb–Br bonds in $[SbBr_6]^{3-}$ octahedra [46]. There are three main peaks in $Cs_3Sb_2Cl_9$ film. The lower frequency peak with the center at 86 cm^{-1} was regarded as the movement of Cl ions

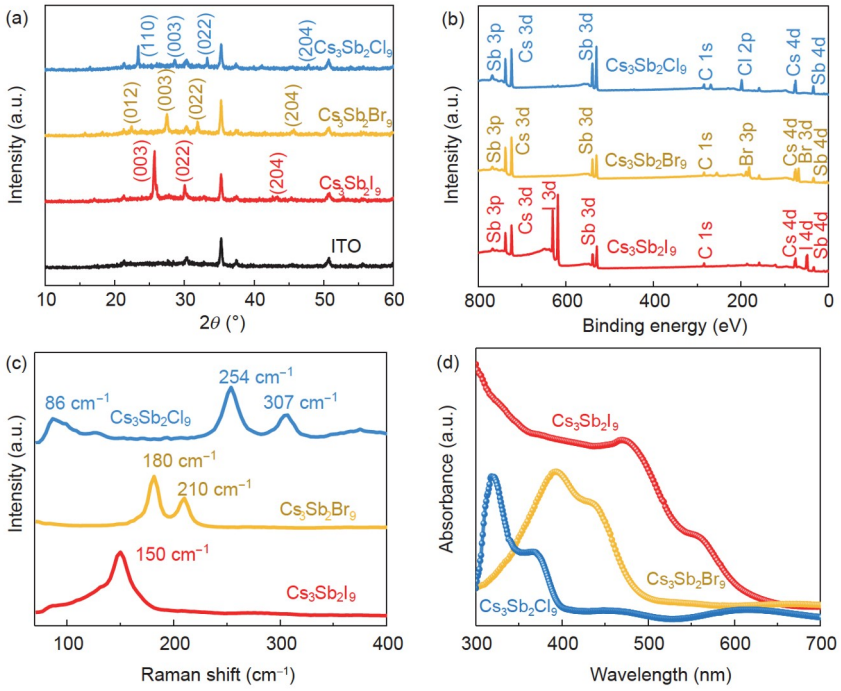

Figure 2 (Color online) (a) XRD patterns of $Cs_3Sb_2X_9$ (X=I, Br, Cl) films; (b) full-range XPS spectrum of $Cs_3Sb_2X_9$ (X=I, Br, Cl) films; (c) Raman spectra of $Cs_3Sb_2X_9$ (X=I, Br, Cl) films; (d) UV-vis spectrum of $Cs_3Sb_2X_9$ (X=I, Br, Cl) films.

[26]. The peaks locating at 254 and 307 cm^{-1} were from the bond vibrations of Cs–Cl and Sb–Cl, respectively [25]. The UV-vis measurements were presented to evaluate optical absorption properties of the $Cs_3Sb_2X_9$ (X=I, Br, Cl) films, as exhibited in Figure 2(d). There were two dominant absorption peaks for all three $Cs_3Sb_2X_9$ (X=I, Br, Cl) films. Compared with $Cs_3Sb_2I_9$, the absorption peaks of $Cs_3Sb_2Br_9$ and $Cs_3Sb_2Cl_9$ films have a clear blue shift [47]. To evaluate the band gap energy (E_g) of $Cs_3Sb_2X_9$ (X=I, Br, Cl) films, the Tauc plot of absorption spectra were drawn in Figure S2. The estimated results of E_g were 2.07, 2.63, and 3.10 eV for $Cs_3Sb_2I_9$, $Cs_3Sb_2Br_9$, and $Cs_3Sb_2Cl_9$ films, respectively [23,47–49]. The surface morphology and elemental mappings for $Cs_3Sb_2X_9$ (X=I, Br, Cl) films were shown in Figure S3. It is found that all three $Cs_3Sb_2X_9$ (X=I, Br, Cl) films featured a uniform size on the substrate surface. Moreover, the homogeneous distributions were observed for all the elements of Cs, Sb, I, Br, and Cl in their individual films.

3.2 Bipolar resistive switching behaviors

Figure 3 shows the *I-V* characteristics of the three types of Al/$Cs_3Sb_2X_9$ (X=I, Br, Cl)/ITO devices, which is measured at room temperature. The solid spheres and the empty circles represent the experimental data of pristine device and the device after 100 days in air, respectively, which manifests the excellent stability for the present Al/$Cs_3Sb_2X_9$/ITO devices. The schematic configurations of the devices were inserted in the left of Figure 3(a)–(c). The positive and negative voltages were applied on the Al and ITO electrodes, respectively. Interestingly, all devices exhibited a bipolar resistive switching behavior by applying scanning voltage of 0 → 1 → 0→ −1.8 → 0 V. The *I-V* properties of Al/$Cs_3Sb_2I_9$/ITO device were plotted in Figure 3(a). The black arrows denote the sweep directions of applied voltage. When the voltage changed from 0 to 1 V, the device remained a low current in the initial stage, corresponding to a high resistive state (HRS). The electronic current abruptly increased at around 0.67 V inducing a low resistive state (LRS) or on-state, which is generally named as the "SET" process, and 0.67 V is defined as V_{SET}. The device then maintained the on-state while the voltage was swept to the reverse direction (+1 to 0 V). The "RESET" procedure appeared under a negative scanning voltage from 0 to −1.8 V. The device remained in the LRS until at a sufficient reverse bias of −1.07 V (V_{RESET}) and then a resistance switched from the LRS to the HRS, corresponding to the off-state. The ratio of currents in the LRS to HRS is referred to the ON/OFF ratio, which is about 10 under the reading voltage of 0.1 V in the Al/$Cs_3Sb_2I_9$/ITO device. As shown in Figure 3(b), the V_{SET} and V_{RESET} were around 0.32 and −0.98 V in the Al/$Cs_3Sb_2Br_9$/ITO device, respectively. The ON/OFF ratio is almost 30 under the reading voltage of 0.1 V in Al/$Cs_3Sb_2Br_9$/ITO device. In contrast, the device performances of the Al/$Cs_3Sb_2Cl_9$/ITO device are very interesting, which showed the V_{SET} and V_{RESET} obviously reduced to around 0.11 and −0.56 V, respectively. Moreover, the ON/OFF ratio under the reading voltage of 0.1 V significantly increased up to 100 in the Al/

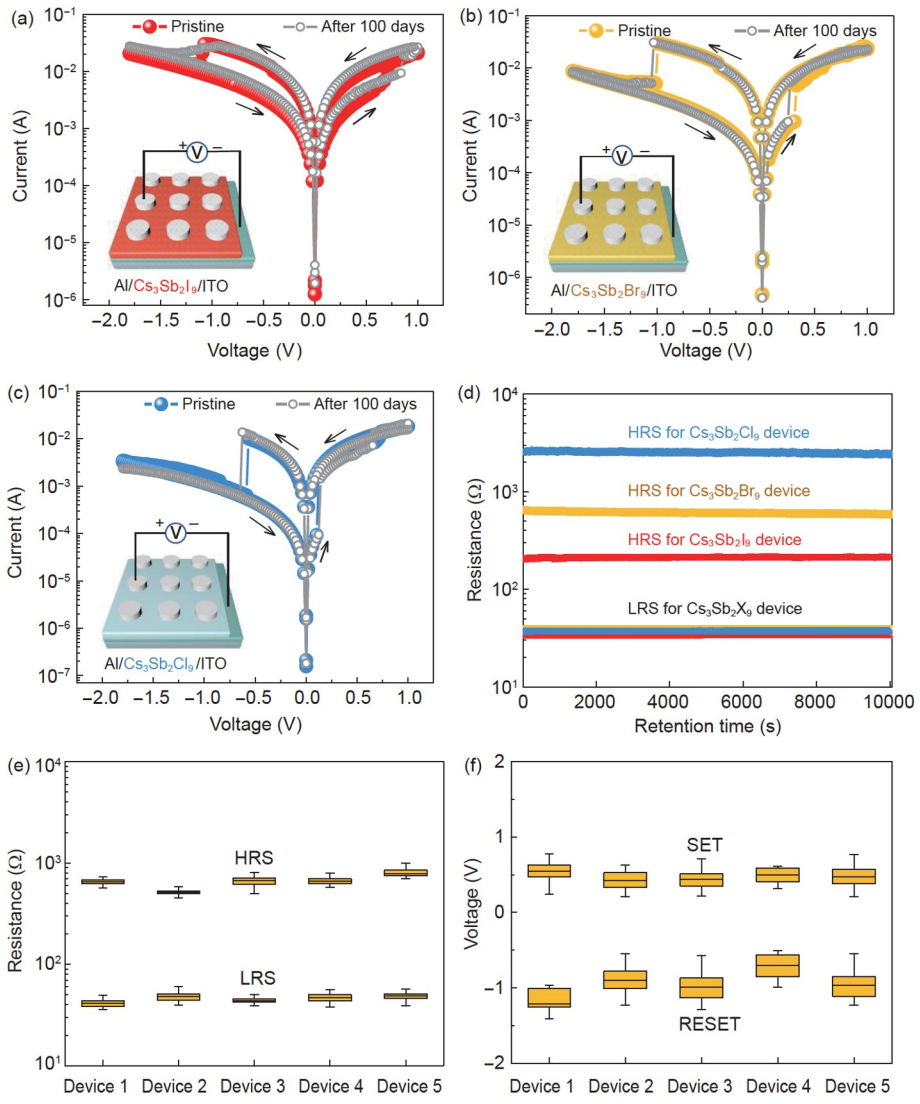

Figure 3 (Color online) *I-V* characteristics of (a) Al/$Cs_3Sb_2I_9$/ITO device, (b) Al/$Cs_3Sb_2Br_9$/ITO device, and (c) Al/$Cs_3Sb_2Cl_9$/ITO device. (d) Retention time test of one Al/$Cs_3Sb_2X_9$ (X=I, Br, Cl)/ITO device. (e) Statistics of the LRS and HRS resistance distributions in five Al/$Cs_3Sb_2Br_9$/ITO devices. (f) Statistics of SET and RESET voltages distributions in five Al/$Cs_3Sb_2Br_9$/ITO devices.

$Cs_3Sb_2Cl_9$/ITO device, which is nearly 10 and 3 times larger than that of the Al/$Cs_3Sb_2I_9$/ITO device and the Al/$Cs_3Sb_2Br_9$/ITO device, respectively, as shown in Figure 3(c). The lower switching voltage and high ON/OFF ratio could be beneficial to the decrease of power consumption and the increase of accuracy for information storage in RRAM devices. In addition, the electrical stability of present Al/$Cs_3Sb_2X_9$ (X=I, Br, Cl)/ITO devices were also evaluated. The retention time and endurance performances were tested under the reading voltage of 0.1 V. As shown in Figure 3(d), neither the HRS nor the LRS of the present Al/$Cs_3Sb_2X_9$ (X=I, Br, Cl)/ITO devices showed obvious fluctuation over the testing period of 10^4 s, indicating the excellent device stability of retention time. Figure S4 showed the endurance performances of Al/$Cs_3Sb_2X_9$ (X=I, Br, Cl)/ITO devices. It was found that the resistances of all devices can be maintained after 750 cycles, and there was no obvious difference during different cycles, as illustrated in Figure S5. The statistics distributions of resistance of HRS and LRS as well as switching voltage distribution from five Al/$Cs_3Sb_2Br_9$/ITO devices were displayed in Figure 3(e) and (f), proving the deviation of the resistance distribution is very small in five devices. The similar resistance distributions of $Cs_3Sb_2I_9$ and $Cs_3Sb_2Cl_9$ memory devices were also shown in Figure S6. The experiments clearly illustrate that the present Al/$Cs_3Sb_2X_9$ (X=I, Br, Cl)/ITO devices have reliable resistive switching behaviors.

It is also noted that the resistance of HRS increases in Al/$Cs_3Sb_2X_9$ (X=I, Br, Cl)/ITO devices as the halide ions changed from I, Br to Cl. A high resistance corresponds to a small free carrier density in the semiconductors, which depends on the relation of $e^{-E_g/kT}$ [50]. Here, T and K are the

absolute temperature and Boltzmann's constant, respectively. The increase of E_g in the $Cs_3Sb_2X_9$ (X=I, Br, Cl) films was demonstrated from I, Br to Cl (Figure S2), thus, the resistance of HRS in Al/$Cs_3Sb_2Cl_9$/ITO device would be the highest. However, the *I-V* characteristics of the LRS region with double-log scale exhibited a slope of ~1 for all three Al/$Cs_3Sb_2X_9$ (X=I, Br, Cl)/ITO devices, demonstrating the transport of electrons obey the Ohmic conduction mechanism ($I \propto V$), as exhibited in Figure S7. So the resistance of LRS for all three devices is nearly same. As a result, the ON/OFF ratio of Al/$Cs_3Sb_2Cl_9$/ITO device will be the highest compared with other two devices.

It is found that the V_{SET} and V_{RESET} in the Al/$Cs_3Sb_2X_9$ (X=I, Br, Cl)/ITO devices gradually decrease as the halide ions changed from I, Br to Cl. The switching voltages strongly rely on the vacancy migration and the lowest activation energy (E_A) decides the vacancy migration rate in perovskite films [51,52]. In $Cs_3Sb_2X_9$ (X=I, Br, Cl) films, the vacancies of Cs and Sb are difficult to be moved because a very huge activation energy would be required [31]. So the vacancies of Cs and Sb could not contribute to the switching voltages. Hence, the migration of $V^{\bullet}_{X\ (X=I,\ Br,\ Cl)}$ should be responsible for different switching voltages in the present Al/$Cs_3Sb_2X_9$ (X=I, Br, Cl)/ITO devices. The E_A of halide vacancies was theoretically calculated based on the DFT by considering a minimum migration path [53]. The calculated lattice parameters of $Cs_3Sb_2X_9$ (X=I, Br, Cl) were list in Table 1, which agree well with the reports in both theorical and experimental results [18,47,54,55]. The layered crystal structure of $Cs_3Sb_2X_9$ (X=I, Br, Cl) can be seen in Figure 4(a). Figure 4(b) shows that the migration path of halide vacancies is along octahedral edge from one halide site to an adjacent one in $Cs_3Sb_2X_9$ (X=I, Br, Cl). As shown in Figure 4(c), the activation energy is 0.23, 0.18, and 0.15 eV for $V^{\bullet}_{I}$, $V^{\bullet}_{Br}$, and $V^{\bullet}_{Cl}$, respectively. The result is similar to the data in previous report [19]. The vacancy migrates more easily with a small activation energy. Correspondingly, the formation and rupture of conductive filament would require a small electric field strength. Thus, the switching voltage of Al/$Cs_3Sb_2Cl_9$/ITO device is the smallest compared with that of the other two devices. This means that the current devices with halide vacancies could potentially be applied under an ultralow electric field strength.

Table 1 Calculated lattice parameters of $Cs_3Sb_2X_9$ (X=I, Br, Cl)

Species		Lattice constants (Å)		
		a	*b*	*c*
$Cs_3Sb_2I_9$	Present	8.662	8.662	10.640
	Theory [47]	8.664	8.664	10.633
	Exp. [54]	8.420	8.420	10.386
$Cs_3Sb_2Br_9$	Present	8.143	8.143	9.979
	Theory [47]	8.138	8.138	9.943
	Exp. [18]	7.930	7.930	9.716

To explore the resistive switching mechanism in the Al/$Cs_3Sb_2X_9$ (X=I, Br, Cl)/ITO devices, the formation and rupture of electric conduction filament owing to the migration of $V^{\bullet}_{X\ (X=I,\ Br,\ Cl)}$ was illustrated in Figure 4(d). In the initial state, the halide vacancies randomly disperse in the $Cs_3Sb_2X_9$ (X=I, Br, Cl) films and the electrons can hardly cross the $Cs_3Sb_2X_9$ (X=I, Br, Cl) films, corresponding to the HRS. When the positive voltages are applied, the halide ions

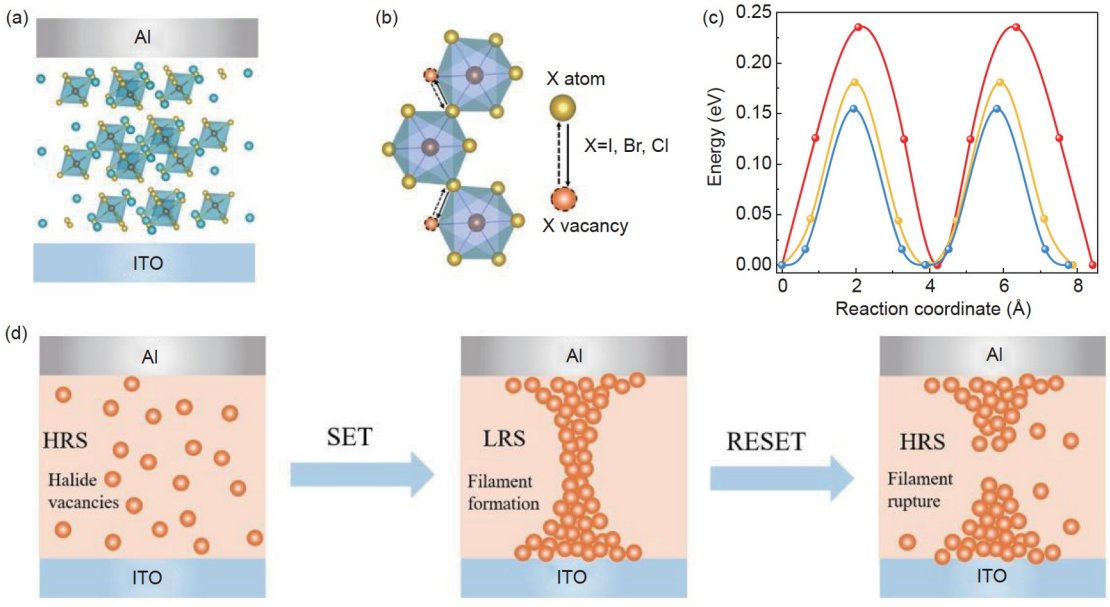

Figure 4 (Color online) (a) Schematic architecture of Al/$Cs_3Sb_2X_9$ (X=I, Br, Cl)/ITO device. (b) Illustration of migration paths for halide X (I, Br, Cl) vacancy in $Cs_3Sb_2X_9$ (X=I, Br, Cl) layers. (c) Activation energy of halide X (I, Br, Cl) vacancies through DFT calculations. (d) The schematic illustration of the resistive switching model.

move and form halide vacancies. The accumulation of vacancies would form the filament. Hence, the electrons could move along the filament of halide vacancies, inducing the LRS, which is the "SET" procedure. When the negative voltages are carried out sequentially, the redistribution of halide vacancies cause the rupture of conduction filament, resulting in the HRS and the "RESET" procedure.

3.3 Artificial synaptic simulations

The conductance state of HRS and LRS in the present Al/$Cs_3Sb_2X_9$ (X=I, Br, Cl)/ITO devices can be used to simulate the characteristics of the biological synaptic function [56,57]. Figure 5(a) describes the corresponding relationship between the structure of biological synapse and the perovskite device. A pulse voltage applied to the Al electrode will induce the migration of halide vacancy in the perovskite layer. As a result, the device conductance would change, which is similar to the change of the connection strength between pre-synapse and post-synapse [58–60]. Either strengthening or weakening the connection of synapses is defined as synaptic plasticity, including the short-term plasticity and long-term plasticity [61,62].

The short-term plasticity is triggered by short-term stimulation, resulting in around milliseconds plasticity changes [62,63]. As shown in Figure 5(b), under the stimulation of a single pulse (0.5 V in amplitude and 20 ms in duration), the conductance responses of Al/$Cs_3Sb_2X_9$ (X=I, Br, Cl)/ITO devices suddenly rise to a larger value, and then slowly decrease. This phenomenon can mimic the excitatory postsynaptic current behavior [60,63]. When two pulses (0.5 V, 20 ms) are continuously applied with an interval time (ΔT) of 20 ms to the Al/$Cs_3Sb_2X_9$ (X=I, Br, Cl)/ITO devices, the conductance excited by the second pulse is larger than that caused by the first pulse, as shown in Figure 5(c). This can simulate paired-pulsed facilitation (PPF) characteristic of synapses. If A_1 and A_2 were the conductance values induced by the first and second pulses, respectively, the PPF index could be calculated as follows:

$$\text{PPF Index}=\frac{A_2-A_1}{A_1}\times 100\%.$$

The calculated results were drawn in Figure 5(d). With the increase of the time interval ΔT, the PPF index gradually goes down, which conforms to biological synaptic characteristics [64,65]. In particular, the Al/$Cs_3Sb_2Cl_9$/ITO device showed the highest PPF index compared to other two devices, which is very interesting and will be further explored in the following long-term plasticity of synapse.

The transition from short-term plasticity to long-term

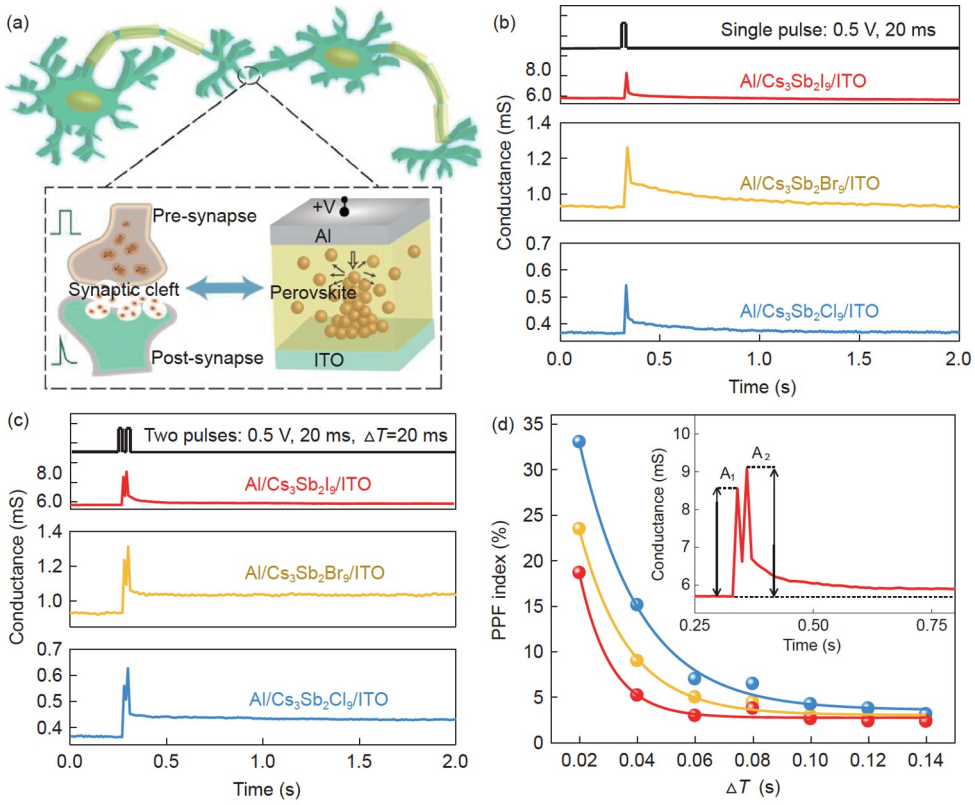

Figure 5 (Color online) (a) Schematics of the relation between biological synapse and architecture of perovskite device. (b) Conductance responses of Al/$Cs_3Sb_2X_9$ (X=I, Br, Cl)/ITO devices under a single pulse (V_{read}=0.1 V). (c) Conductance responses of Al/$Cs_3Sb_2X_9$ (X=I, Br, Cl)/ITO devices under two pulses (V_{read}=0.1 V and ΔT=20 ms). (d) The dependence of PPF index on ΔT in the Al/$Cs_3Sb_2X_9$ (X=I, Br, Cl)/ITO devices. A_1 and A_2 in the inset represent the conductance response of the first and second pulses, respectively.

plasticity can be achieved through repetitive rehearsal of electrical stimuli with the same pulse [12,57,66]. The long-term plasticity of synapse consists of long-term potentiation (LTP) and long-term depression (LTD) [67,68]. The spike-timing-dependent plasticity (STDP) can describe the relationship between LTP, LTD, and the time difference (Δt) of pre-synaptic/post-synaptic pulses [69,70]. Here, by controlling the value of Δt, the STDP was studied in the current Al/$Cs_3Sb_2Cl_9$/ITO device, as shown in Figure 6(a). The applied pre- and post-synaptic pulses were shown in the inset of Figure 6(a). When the pre-synaptic pulse is triggered before the post-synaptic pulse ($\Delta t>0$), the LTP appeared in the device, and the relative change of the synaptic weight ($\Delta G/G_{pre}$) clearly reduced with the increase of Δt. On the contrary, LTD would be present when the pre-synaptic pulse arrived after the post-synaptic pulse ($\Delta t<0$). The dependences of $\Delta G/G_{pre}$ on Δt could be fitted by the exponential functions [71,72]:

$$\Delta G = G_{post} - G_{pre},$$

$$\frac{\Delta G^+}{G_{pre}} = A^+ \exp\left(-\frac{\Delta t}{\tau^+}\right); \Delta t > 0,$$

$$\frac{\Delta G^-}{G_{pre}} = A^- \exp\left(\frac{\Delta t}{\tau^-}\right); \Delta t < 0,$$

where G_{pre} and G_{post} are the conductance of the pre-synapse and post-synapse for the Al/$Cs_3Sb_2Cl_9$/ITO device, A and τ are the amplitude parameter and time constant, respectively. The fitted results of τ^+ and τ^- values are 6.84 and 8.37 ms, respectively, which are comparable to the millisecond-scale response time in biological synapses [12]. Moreover, the data was well fitted by the above exponential functions, confirming the Al/$Cs_3Sb_2Cl_9$/ITO device could accurately simulate the antisymmetric Hebbian learning rules. Furthermore, the conductance values during 5 continuous cycles of potentiation and depression processes were drawn in Figure 6(b), which was evaluated under 25 positive (+0.5 V, 20 ms) and 25 negative (−0.5 V, 20 ms) pulses for each cycle. The results clearly testify the excellent response reproducibility and stability of the current Al/$Cs_3Sb_2Cl_9$/ITO device.

As plotted in Figure 6(c), the preliminary learning behaviors of synapses "Learning, Forgetting, and Re-Learning" processes were evaluated using the Al/$Cs_3Sb_2Cl_9$/ITO device to emulate the memory function of human brain. First, 100 consecutive pulses (0.5 V, 20 ms) were applied to the device for mimicking the "Learning" process. The conductance obviously increased with increasing the numbers of voltage pulse, indicating that the information was remembered. As shown in the middle panel of Figure 6(c), the device conductance gradually decayed after the voltage pulse was

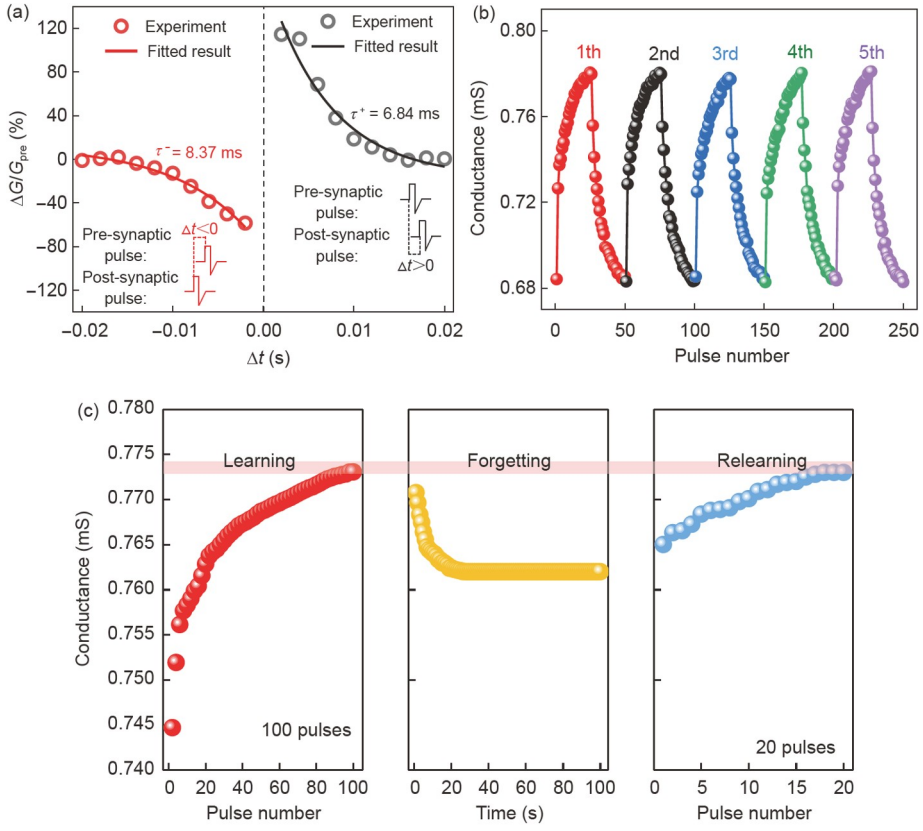

Figure 6 (Color online) (a) The dependences of $\Delta G/G_{pre}$ on time difference (Δt) with pre-synaptic/post-synaptic pulses from one Al/$Cs_3Sb_2Cl_9$/ITO device. (b) The change of conductance with five continuous cycles for the Al/$Cs_3Sb_2Cl_9$/ITO device under the reading pulse of 0.1 V. (c) The simulation of learning, forgetting and relearning processes with the voltage (0.5 V, 20 ms) using the Al/$Cs_3Sb_2Cl_9$/ITO device under the reading pulse of 0.1 V.

removed. Compared this to the result in the left panel of Figure 6(c), the conductance state does not completely decay back to the original one even after 100 s, meaning the partial information was forgotten and the other part of the information was converted into long-term memory [73]. This could simulate the Ebbinghaus forgetting process [74,75]. Finally, the conductance was recovered to the learning level before spontaneous decay by applying only 20 consecutive pulses (0.5 V, 20 ms), which is analogous to the "Relearning" process of human brains.

The ability of associative learning, in which related things are linked together, plays a key role in the cognitive functions of biological systems, and is known as Pavlovian conditioning or classical conditioning [76,77]. Thus, the present Al/$Cs_3Sb_2Cl_9$/ITO device simulated the Pavlov' dog experiment, as shown in Figure 7. Here, a single voltage pulse (0.5 V, 10 ms) and a voltage pulse (0.5 V, 10 ms) with light illumination represented the bell signal and food signal, respectively. The conductance of 0.3 mS of the device was set as the threshold of salivation, meaning that a conductance beyond the threshold value represents the salivation behavior of the dog. During the first stage (0–1 s), the 100 voltage pulses (bell signals) were applied to the device. The conductance was lower than 0.3 mS, meaning that the dog would not salivate. In second stage (1–2 s), when the 100 voltage pulses with light illumination (food signals) were applied to the device, the conductance broke the threshold of 0.3 mS. Thus, the dog would show the salivation behavior. Next, when both the bell and food signals were applied to the device simultaneously, the conductance increased greatly and broke the threshold of salivation, corresponding to the "Training" process (2–3 s). After the training process, only a bell signals (3–4 s) can also trigger the salivation of dog, illustrating that the device possessed an efficient association between the bell and food. Finally, if the training was stopped, only a bell signal no longer caused the dog to salivate, demonstrating that the associative learning behavior was forgotten by the dog over time. According to the above experimental results, the current Al/$Cs_3Sb_2Cl_9$/ITO device could successfully simulate Pavlov's dog experiment and established associative learning behavior. Compared the voltage pulse (0.5 V, 20 ms) used in Figures 5 and 6, a shorter pulse in duration (0.5 V, 10 ms) of Figure 7 proves a faster learning behavior of synaptic simulation using the present devices, which is beneficial to reduce the power consumption [5,74,77]. In addition, the memory devices based on lead free perovskites have been summarized in Table S1. It can be concluded that the present Al/$Cs_3Sb_2X_9$ (X=I, Br, Cl)/ITO devices showed a competitive performance in resistive switching behavior and artificial synaptic simulation.

4 Conclusion

The RRAM devices based on antimony-based $Cs_3Sb_2X_9$ (X=I, Br, Cl) thin films were successfully prepared, exhibiting bipolar resistive switching and artificial synaptic behaviors. Particularly, the $Cs_3Sb_2Cl_9$ device showed a long endurance up to 750 cycles, low switching voltage below 0.6 V, and long retention time over 10^4 s. The decrease of switching voltages of Al/$Cs_3Sb_2X_9$ (X=I, Br, Cl)/ITO devices with the X from I, Br to Cl could be explained by the consecutive decrease of activation energy of halide vacancies in the $Cs_3Sb_2X_9$ (X=I, Br, Cl) films. In addition, the short-term plasticity and long-term plasticity of biological synapse as

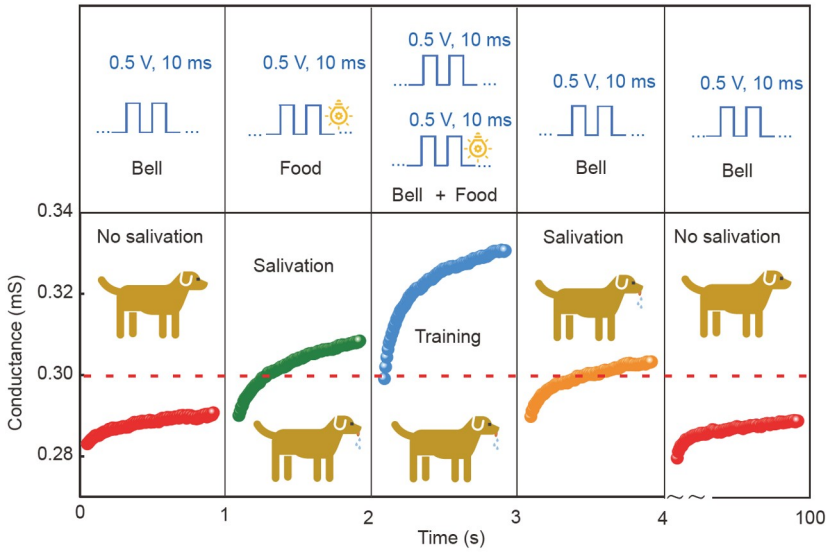

Figure 7 (Color online) Simulation of Pavlov's dog experiment using the Al/$Cs_3Sb_2Cl_9$/ITO devices. A voltage pulse is 0.5 V at 10 ms. V_{read} is 0.1 V and the light intensity is 1.5 mW/cm^2.

well as experience learning processes for the memory ability of human brain were successfully simulated by the present devices. Finally, the present device established associative learning behavior successfully by simulating the Pavlov's dog experiment. This investigation is beneficial to the development of dual-functional devices with non-volatile information storage and artificial synaptic.

This work was supported by the National Natural Science Foundation of China (Grant Nos. 51971057 and 52271238), the Liaoning Revitalization Talents Program (Grant No. XLYC2002075), and the Research Funds for the Central University (Grant Nos. N2202004 and N2102012).

Supporting information

The supporting information is available online at tech.scichina.com and link.springer.com. The supporting materials are published as submitted, without typesetting or editing. The responsibility for scientific accuracy and content remains entirely with the authors.

1 Zidan M A, Strachan J P, Lu W D. The future of electronics based on memristive systems. Nat Electron, 2018, 1: 22–29
2 Hwang B, Lee J S. Recent advances in memory devices with hybrid materials. Adv Electron Mater, 2019, 5: 1800519
3 Kang K, Hu W, Tang X. Halide perovskites for resistive switching memory. J Phys Chem Lett, 2021, 12: 11673–11682
4 Lanza M, Waser R, Ielmini D, et al. Standards for the characterization of endurance in resistive switching devices. ACS Nano, 2021, 15: 17214–17231
5 Xu W, Cho H, Kim Y H, et al. Organometal halide perovskite artificial synapses. Adv Mater, 2016, 28: 5916–5922
6 Xiao Z, Huang J. Energy-efficient hybrid perovskite memristors and synaptic devices. Adv Electron Mater, 2016, 2: 1600100
7 Bisquert J, Guerrero A. Dynamic instability and time domain response of a model halide perovskite memristor for artificial neurons. J Phys Chem Lett, 2022, 13: 3789–3795
8 Luo F, Ruan L, Tong J, et al. Enhanced resistive switching performance in yttrium-doped $CH_3NH_3PbI_3$ perovskite devices. Phys Chem Chem Phys, 2021, 23: 21757–21768
9 Kang K, Ahn H, Song Y, et al. High-performance solution-processed organo-metal halide perovskite unipolar resistive memory devices in a cross-bar array structure. Adv Mater, 2019, 31: 1804841
10 Zheng Y, Luo F, Ruan L, et al. A facile fabrication of lead-free Cs_2NaBiI_6 double perovskite films for memory device application. J Alloys Compd, 2022, 909: 164613
11 Ren Y, Ma H, Wang W, et al. Cycling-induced degradation of organic-inorganic perovskite-based resistive switching memory. Adv Mater Technol, 2019, 4: 1800238
12 Kim S G, Van Le Q, Han J S, et al. Dual-phase all-inorganic cesium halide perovskites for conducting-bridge memory-based artificial synapses. Adv Funct Mater, 2019, 29: 1906686
13 Liu Q, Gao S, Xu L, et al. Nanostructured perovskites for nonvolatile memory devices. Chem Soc Rev, 2022, 51: 3341–3379
14 Sun Y, Tai M, Song C, et al. Competition between metallic and vacancy defect conductive filaments in a $CH_3NH_3PbI_3$-based memory device. J Phys Chem C, 2018, 122: 6431–6436
15 Zhu X, Lee J, Lu W D. Iodine vacancy redistribution in organic-inorganic halide perovskite films and resistive switching effects. Adv Mater, 2017, 29: 1700527
16 Kim D J, Tak Y J, Kim W G, et al. Resistive switching properties through iodine migrations of a hybrid perovskite insulating layer. Adv Mater Interfaces, 2017, 4: 1601035
17 Choi J, Park S, Lee J, et al. Organolead halide perovskites for low operating voltage multilevel resistive switching. Adv Mater, 2016, 28: 6562–6567
18 Zhang J, Yang Y, Deng H, et al. High quantum yield blue emission from lead-free inorganic antimony halide perovskite colloidal quantum dots. ACS Nano, 2017, 11: 9294–9302
19 Mao J Y, Zheng Z, Xiong Z Y, et al. Lead-free monocrystalline perovskite resistive switching device for temporal information processing. Nano Energy, 2020, 71: 104616
20 Singh A, Chiu N C, Boopathi K M, et al. Lead-free antimony-based light-emitting diodes through the vapor–anion-exchange method. ACS Appl Mater Interfaces, 2019, 11: 35088–35094
21 Ma Z, Shi Z, Yang D, et al. Electrically-driven violet light-emitting devices based on highly stable lead-free perovskite $Cs_3Sb_2Br_9$ quantum dots. ACS Energy Lett, 2020, 5: 385–394
22 Yao M M, Jiang C H, Yao J S, et al. General synthesis of lead-free metal halide perovskite colloidal nanocrystals in 1-dodecanol. Inorg Chem, 2019, 58: 11807–11818
23 Lu C, Itanze D S, Aragon A G, et al. Synthesis of lead-free $Cs_3Sb_2Br_9$ perovskite alternative nanocrystals with enhanced photocatalytic CO_2 reduction activity. Nanoscale, 2020, 12: 2987–2991
24 Zheng Z, Hu Q, Zhou H, et al. Submillimeter and lead-free $Cs_3Sb_2Br_9$ perovskite nanoflakes: Inverse temperature crystallization growth and application for ultrasensitive photodetectors. Nanoscale Horiz, 2019, 4: 1372–1379
25 Pradhan B, Kumar G S, Sain S, et al. Size tunable cesium antimony chloride perovskite nanowires and nanorods. Chem Mater, 2018, 30: 2135–2142
26 Pradhan A, Sahoo S C, Sahu A K, et al. Effect of Bi substitution on $Cs_3Sb_2Cl_9$: Structural phase transition and band gap engineering. Cryst Growth Des, 2020, 20: 3386–3395
27 Wang X, Ali N, Bi G, et al. Lead-free antimony halide perovskite with heterovalent Mn^{2+} doping. Inorg Chem, 2020, 59: 15289–15294
28 Saparov B, Hong F, Sun J P, et al. Thin-film preparation and characterization of $Cs_3Sb_2I_9$: A lead-free layered perovskite semiconductor. Chem Mater, 2015, 27: 5622–5632
29 Correa-Baena J P, Nienhaus L, Kurchin R C, et al. A-site cation in inorganic $A_3Sb_2I_9$ perovskite influences structural dimensionality, exciton binding energy, and solar cell performance. Chem Mater, 2018, 30: 3734–3742
30 Umar F, Zhang J, Jin Z, et al. Dimensionality controlling of $Cs_3Sb_2I_9$ for efficient all-inorganic planar thin film solar cells by HCl-assisted solution method. Adv Opt Mater, 2019, 7: 1801368
31 Singh A, Boopathi K M, Mohapatra A, et al. Photovoltaic performance of vapor-assisted solution-processed layer polymorph of $Cs_3Sb_2I_9$. ACS Appl Mater Interfaces, 2018, 10: 2566–2573
32 Singh A, Najman S, Mohapatra A, et al. Modulating performance and stability of inorganic lead-free perovskite solar cells via lewis-pair mediation. ACS Appl Mater Interfaces, 2020, 12: 32649–32657
33 Paramanik S, Maiti A, Chatterjee S, et al. Large resistive switching and artificial synaptic behaviors in layered $Cs_3Sb_2I_9$ Lead-free perovskite memory devices. Adv Elect Mater, 2022, 8: 2100237
34 Kresse G. *Ab initio* molecular dynamics for liquid metals. J Non Cryst Solids, 1995, 192-193: 222–229
35 Kresse G, Furthmüller J. Efficient iterative schemes for *ab initio* total-energy calculations using a plane-wave basis set. Phys Rev B, 1996, 54: 11169–11186
36 Kresse G, Furthmüller J. Efficiency of *ab-initio* total energy calculations for metals and semiconductors using a plane-wave basis set. Comput Mater Sci, 1996, 6: 15–50
37 Blöchl P E. Projector augmented-wave method. Phys Rev B, 1994, 50: 17953–17979
38 Kresse G, Joubert D. From ultrasoft pseudopotentials to the projector augmented-wave method. Phys Rev B, 1999, 59: 1758–1775
39 Perdew J P, Burke K, Ernzerhof M. Generalized gradient approximation made simple. Phys Rev Lett, 1996, 77: 3865–3868
40 Perdew J P, Ruzsinszky A, Csonka G I, et al. Restoring the density-gradient expansion for exchange in solids and surfaces. Phys Rev Lett, 2008, 100: 136406

41 Henkelman G, Jóhannesson G, Jónsson H. Methods for finding saddle points and minimum energy paths. In: Schwartz S D (ed). Theoretical Methods in Condensed Phase Chemistry. Progress in Theoretical Chemistry and Physics. Vol 5. Dordrecht: Springer, 2002. 269–302
42 Monkhorst H J, Pack J D. Special points for Brillouin-zone integrations. Phys Rev B, 1976, 13: 5188–5192
43 Chonamada T D, Dey A B, Santra P K. Degradation Studies of $Cs_3Sb_2I_9$: A lead-free perovskite. ACS Appl Energy Mater, 2020, 3: 47–55
44 Singh A, Lai P T, Mohapatra A, et al. Panchromatic heterojunction solar cells for Pb-free all-inorganic antimony based perovskite. Chem Eng J, 2021, 419: 129424
45 Boopathi K M, Karuppuswamy P, Singh A, et al. Solution-processable antimony-based light-absorbing materials beyond lead halide perovskites. J Mater Chem A, 2017, 5: 20843–20850
46 Long N, Lin C, Chen F, et al. Nanocrystallization of lead-free $Cs_3Sb_2Br_9$ perovskites in chalcogenide glass. J Am Ceram Soc, 2020, 103: 6106–6111
47 Liu Y L, Yang C L, Wang M S, et al. Theoretical insight into the optoelectronic properties of lead-free perovskite derivatives of $Cs_3Sb_2X_9$ (X = Cl, Br, I). J Mater Sci, 2019, 54: 4732–4741
48 Timmermans C W M, Cholakh S O, Blasse G. The luminescence of $Cs_3Bi_2Cl_9$ and $Cs_3Sb_2Cl_9$. J Solid State Chem, 1983, 46: 222–233
49 Geng T, Ma Z, Chen Y, et al. Bandgap engineering in two-dimensional halide perovskite $Cs_3Sb_2I_9$ nanocrystals under pressure. Nanoscale, 2020, 12: 1425–1431
50 Muthu C, Agarwal S, Vijayan A, et al. Hybrid perovskite nanoparticles for high-performance resistive random access memory devices: Control of operational parameters through chloride doping. Adv Mater Interfaces, 2016, 3: 1600092
51 Hwang B, Gu C, Lee D, et al. Effect of halide-mixing on the switching behaviors of organic-inorganic hybrid perovskite memory. Sci Rep, 2017, 7: 43794
52 Meloni S, Moehl T, Tress W, et al. Ionic polarization-induced current-voltage hysteresis in $CH_3NH_3PbX_3$ perovskite solar cells. Nat Commun, 2016, 7: 10334
53 Haruyama J, Sodeyama K, Han L, et al. First-principles study of ion diffusion in perovskite solar cell sensitizers. J Am Chem Soc, 2015, 137: 10048–10051
54 Yamada K, Sera H, Sawada S, et al. Reconstructive phase transformation and kinetics of $Cs_3Sb_2I_9$ by means of rietveld analysis of X-ray diffraction and127I NQR. J Solid State Chem, 1997, 134: 319–325
55 Paul S, Sain S, Kamilya T, et al. Shape tunable two-dimensional ligand-free cesium antimony chloride perovskites. Mater Today Chem, 2022, 23: 100641
56 Lao J, Xu W, Jiang C, et al. Artificial synapse based on organic-inorganic hybrid perovskite with electric and optical modulation. Adv Electron Mater, 2021, 7: 2100291
57 Lao J, Xu W, Jiang C, et al. An air-stable artificial synapse based on a lead-free double perovskite $Cs_2AgBiBr_6$ film for neuromorphic computing. J Mater Chem C, 2021, 9: 5706–5712
58 Das U, Sarkar P, Paul B, et al. Halide perovskite two-terminal analog memristor capable of photo-activated synaptic weight modulation for neuromorphic computing. Appl Phys Lett, 2021, 118: 182103
59 Kim S I, Lee Y, Park M H, et al. Dimensionality dependent plasticity in halide perovskite artificial synapses for neuromorphic computing. Adv Electron Mater, 2019, 5: 1900008
60 Kim S J, Lee T H, Yang J M, et al. Vertically aligned two-dimensional halide perovskites for reliably operable artificial synapses. Mater Today, 2022, 52: 19–30
61 Mori M, Abegg M H, Gähwiler B H, et al. A frequency-dependent switch from inhibition to excitation in a hippocampal unitary circuit. Nature, 2004, 431: 453–456
62 Park Y, Kim M K, Lee J S. 2D layered metal-halide perovskite/oxide semiconductor-based broadband optoelectronic synaptic transistors with long-term visual memory. J Mater Chem C, 2021, 9: 1429–1436
63 Hao D, Zhang J, Dai S, et al. Perovskite/organic semiconductor-based photonic synaptic transistor for artificial visual system. ACS Appl Mater Interfaces, 2020, 12: 39487–39495
64 Hu S G, Liu Y, Chen T P, et al. Emulating the paired-pulse facilitation of a biological synapse with a NiO_x-based memristor. Appl Phys Lett, 2013, 102: 183510
65 Liu G, Wang C, Zhang W, et al. Organic biomimicking memristor for information storage and processing applications. Adv Electron Mater, 2016, 2: 1500298
66 Wang W, Gao S, Li Y, et al. Artificial optoelectronic synapses based on TiN_xO_{2-x}/MoS_2 heterojunction for neuromorphic computing and visual system. Adv Funct Mater, 2021, 31: 2101201
67 Engert F, Bonhoeffer T. Dendritic spine changes associated with hippocampal long-term synaptic plasticity. Nature, 1999, 399: 66–70
68 Du C, Ma W, Chang T, et al. Biorealistic implementation of synaptic functions with oxide memristors through internal ionic dynamics. Adv Funct Mater, 2015, 25: 4290–4299
69 Huang W, Xia X, Zhu C, et al. Memristive artificial synapses for neuromorphic computing. Nano-Micro Lett, 2021, 13: 85
70 Kwak K J, Lee D E, Kim S J, et al. Halide perovskites for memristive data storage and artificial synapses. J Phys Chem Lett, 2021, 12: 8999–9010
71 Li J, Ge C, Lu H, et al. Energy-efficient artificial synapses based on oxide tunnel junctions. ACS Appl Mater Interfaces, 2019, 11: 43473–43479
72 Liu L, Cheng Z, Jiang B, et al. Optoelectronic artificial synapses based on two-dimensional transitional-metal trichalcogenide. ACS Appl Mater Interfaces, 2021, 13: 30797–30805
73 Ohno T, Hasegawa T, Tsuruoka T, et al. Short-term plasticity and long-term potentiation mimicked in single inorganic synapses. Nat Mater, 2011, 10: 591–595
74 Ku B, Koo B, Sokolov A S, et al. Two-terminal artificial synapse with hybrid organic-inorganic perovskite $(CH_3NH_3)PbI_3$ and low operating power energy (~47 fJ/μm^2). J Alloys Compd, 2020, 833: 155064
75 Liu J, Yang Z, Gong Z, et al. Weak light-stimulated synaptic hybrid phototransistors based on islandlike perovskite films prepared by spin coating. ACS Appl Mater Interfaces, 2021, 13: 13362–13371
76 Subramanian Periyal S, Jagadeeswararao M, Ng S E, et al. Halide perovskite quantum dots photosensitized-amorphous oxide transistors for multimodal synapses. Adv Mater Technol, 2020, 5: 2000514
77 Gong J, Wei H, Ni Y, et al. Methylammonium halide-doped perovskite artificial synapse for light-assisted environmental perception and learning. Mater Today Phys, 2021, 21: 100540